

# High-resolution optical diffraction microscopy

Kamal Belkebir and Anne Sentenac

*Institut Fresnel, Centre National de Recherche Scientifique, Unit Mixte de Recherche 6133, Campus de Saint Jérôme, case 162, 13397 Marseille Cedex, France*

Received October 10, 2002; revised manuscript received February 25, 2003; accepted March 3, 2003

In an optical diffraction microscopy experiment, one measures the phase and amplitude of the field diffracted by the sample and uses an inversion algorithm to reconstruct its map of permittivity. We show that with an iterative procedure accounting for multiple scattering, it is possible to visualize details smaller than  $\lambda/4$  with relatively few illumination and observation angles. The roles of incident evanescent waves and noise are also investigated. © 2003 Optical Society of America

OCIS codes: 180.6900, 110.6960, 290.3200.

## 1. INTRODUCTION

The need for new visualization tools with sub-100-nm resolution is anticipated in various scientific fields. In biology, the three-dimensional morphologic observation of the cell and its nucleus below 100 nm is now required for the understanding of the different exchange mechanisms. In semiconductor industries, the technology of silicon integrated circuits has reached process size scales of the order of 0.1 micrometer, which necessitates high-resolution, three-dimensional (3D) imaging systems for performing nondestructive inspection of the wafers.

Several types of apparatus such as electronic microscopes and atomic force microscopes have resolution smaller than a nanometer. Yet they are devoted solely to surface imaging, 3D reconstruction being possible only by cutting slices of the sample. Optical near-field microscopy also presents a power of resolution smaller than 100 nm, and it is potentially useful for 3D imaging.<sup>1</sup> While quite promising, this technique requires the manipulation of a probe in the vicinity (within a few nanometers) of the object, which is not always convenient, in particular for *in vivo* imaging.

Optical far-field microscopes, on the other hand, permit the investigator to obtain 3D images without being invasive, by focusing on different planes of the sample. Their resolution is limited by the axial and lateral widths of their point-spread function,<sup>2,3</sup> which depends on the numerical aperture of the objectives. In classic microscopes, the resolution is typically one micrometer laterally and several micrometers axially. Considerable work has been done to ameliorate the effects of the point-spread function. The lateral resolution has been improved by increasing the collected solid angle or, equivalently (by means of the reciprocity theorem<sup>4</sup>), by increasing the illumination solid angle. This can be done by immersing the objective in a liquid with a high refractive index. Another method uses a hemispherical prism, either to collect the scattered light, as in subsurface microscopy,<sup>5</sup> or to illuminate the sample, as in total internal microscopy.<sup>6</sup> The axial power of resolution has also been drastically improved by using an objective placed on each side of the sample, thus doubling the solid angle of

collection and illumination. Distance separations smaller than 200 nm have been reported in all three directions with the best fluorescence microscopes.<sup>7</sup>

A novel imaging technique known as optical diffraction tomography (ODT) is now addressing the issue of 3D imaging with subwavelength resolution. It consists in illuminating the sample from many different directions and collecting the diffracted field under many scattered angles. In contrast to optical microscopy, in which the object is visualized in an analogical way with little or no numerical treatment for deblurring the image, ODT relies entirely on a numerical inverse procedure for reconstructing the map of permittivity of the sample from the data of the scattered field. For some time, this technique has been limited to the study of absorbing objects whose typical length scale is much larger than the wavelength. In the short-wavelength limit, the reconstruction algorithms use a geometrical ray model of propagation inspired by that developed in x-ray tomography, and only intensity measurements are necessary for retrieving the 3D variations of the absorption in the sample. When the features of the object of interest are of the same order as the wavelength, one must take scattering into account. In this case, although some reconstruction algorithms using intensity data only have been proposed,<sup>8</sup> most inverse procedures require amplitude and phase measurements. The difficulty of measuring the phase in optics has certainly hindered the development of ODT. Different interferometric setups, such as phase-shifting holography and heterodyne holography, give valuable information on the phase and amplitude of the scattered field, but the control of the phase of the incident beam when several illumination angles are required is very difficult. In many studies, only one incident direction is used, which limits the power of resolution of the technique. Other approaches that use in-line holography permit one to use successive illuminations by inferring the phase from the interferogram through extensive processing of the data. In the past ten years, several ODT experiments have been conducted with a resolution of the order of the wavelength. Very recently, a means of compensating for the uncontrolled phase shift in a phase-shifting holography setup

has been proposed.<sup>9</sup> It has permitted performance of ODT with a large number of successive illumination beams and the attainment with accuracy of the phase and amplitude of the scattered field. As a result, the resolution of the images has been improved by up to a quarter of the wavelength.

Most inversion procedures used in ODT experiments are based on the Rytov or Born approximations under which the 3D Fourier components of a 3D scatterer are obtained from the two-dimensional (2D) Fourier components of the scattered field<sup>10</sup> by changing the angle of the incident plane wave. The reconstruction of the map of permittivity is then performed with a simple Fourier transform. To compensate for the missing cones in the Fourier space attributable to the limited solid angle of collection and illumination, reconstruction procedures that use interpolation techniques, backpropagation algorithms, and least-squares minimizations have been developed.<sup>6,11</sup> These methods, which are used in many fields of physics in acoustic or microwave domains, prove to be robust with respect to noise. They are justified when there is a linear relationship between the scattered field and the Fourier components of the permittivity, i.e., under a weak-scattering approximation. However, this assumption limits the field of application of ODT. Now in microwave domains, inverse scattering problems have been addressed with iterative methods that account for multiple scattering and improve the result of linear inversions.<sup>12,13</sup>

We present an iterative method of reconstruction whose first step is the classic backpropagation algorithm. We adapt it to the configuration of ODT in transmission<sup>9</sup> and total internal microscopy.<sup>1</sup> We show that a resolution below  $\lambda/4$  in the lateral and axial directions can be anticipated with relatively few illuminations and far-field measurements. The sensitivity of the reconstruction to noise is also addressed.

## 2. CONFIGURATION OF THE EXPERIMENT

The illumination and detection configurations under consideration here are typical of what can be done in a transmission diffraction tomography experiment<sup>9</sup> in which both the phase and the amplitude of the diffracted field are measured.

### A. Presentation of the Structure

The structure consists of two cylinders with rectangular cross section deposited on a semi-infinite substrate as shown in Fig. 1. The geometry is invariant along the  $Oy$  axis. The width of the rectangles along the  $Ox$  axis is  $\lambda/6$  as is the distance separating the two cylinders. Hereafter,  $\lambda$  is the wavelength of the incident beam in vacuum. The height along  $Oz$  of the first rectangle is  $\lambda/6$  while that of the second rectangle is  $\lambda/3$ . The height difference is a means of testing the accuracy of the reconstruction in the axial direction. The separation distance and the lateral widths of the cylinders will give insight on lateral resolution. Both cylinders and substrate are homogeneous with permittivity  $\varepsilon_b = 2.25$ . The superstrate is air. We call  $\varepsilon(x, z)$  the permittivity of the whole geometry. For convenience, we introduce  $\varepsilon_r(z)$ , the permittivity of the

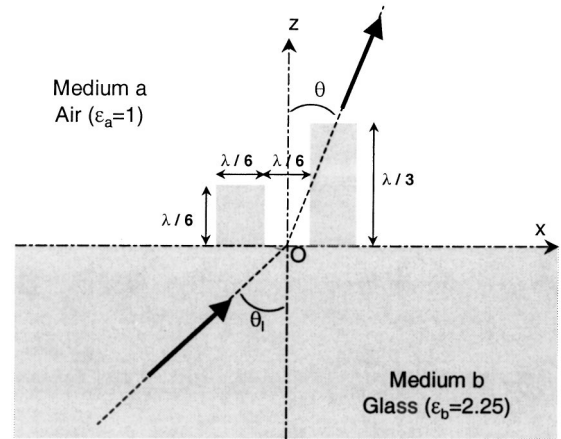


Fig. 1. Geometry of the problem.

reference geometry without the cylinders;  $\varepsilon_r(z) = \varepsilon_b$  for  $z < 0$  and  $\varepsilon_r(z) = 1$  for  $z \geq 0$ . The perturbation introduced by the cylinders is described by the contrast of permittivity  $\chi(x, z) = \varepsilon(x, z) - \varepsilon_r(z)$ . Hereafter, we note  $\mathbf{r} = (x, z)$ .

The object is illuminated by a plane wave coming from the substrate in the plane orthogonal to  $Oy$  with angle  $\theta_i$  with respect to the  $Oz$  axis. This plane wave can either be transmitted into the superstrate or totally reflected at the interface. All the electric fields are directed along the  $Oy$  axis so we consider only scalar equations. We measure the phase and amplitude of the scattered field in the superstrate along the direction defined by the angle  $\theta$  in Fig. 1.

### B. Volume Integral Representation of the Field

Throughout the paper, a time dependence on  $\exp(-i\omega t)$  is assumed and ignored. The  $y$  component of the electric field  $E_l$  satisfies the Helmholtz equation

$$\Delta E_l(\mathbf{r}) + \varepsilon_r(z)k_0^2 E_l(\mathbf{r}) = S_l - k_0^2 \chi(\mathbf{r})E_l(\mathbf{r}), \quad (1)$$

where  $k_0 = 2\pi/\lambda$  is the wave number in vacuum and  $S_l$  is the source that radiates the incident beam. The subscript  $l$  in  $E_l$  indicates the dependence of the electric field on the incident field generated by  $S_l$ . Introducing the Green's-function solution of

$$\Delta G(\mathbf{r}, \mathbf{r}') + \varepsilon(z)k_0^2 G(\mathbf{r}, \mathbf{r}') = -\delta(\mathbf{r} - \mathbf{r}') \quad (2)$$

that satisfies the outgoing-wave boundary condition, one can rewrite the differential equation (1) into an integral equation

$$E_l(\mathbf{r}) = E_l^{\text{ref}}(\mathbf{r}) + k_0^2 \int_{\Omega} G(\mathbf{r}, \mathbf{r}') \chi(\mathbf{r}') E_l(\mathbf{r}') d\mathbf{r}', \quad (3)$$

where  $E_l^{\text{ref}}$  is the field that would exist in the reference geometry and  $\Omega$  is the domain where the contrast of permittivity is not null. When the incident beam is a plane wave coming from the substrate with amplitude unity and angle of incidence  $\theta_i$ , then, for  $z > 0$ ,  $E_l^{\text{ref}}$  is the Fresnel transmitted plane wave,

$$E_l^{\text{ref}}(\mathbf{r}) = t(\kappa_l) \exp(i\kappa_l x + i\gamma_l z), \quad (4)$$

and, for  $z < 0$ , the sum of the incident and specularly reflected field in the substrate,

$$E_l^{\text{ref}}(\mathbf{r}) = \exp(i\kappa_l x + i\gamma_l^b z) + r(\kappa_l) \exp(i\kappa_l x - i\gamma_l^b z), \quad (5)$$

where  $\kappa_l = \sqrt{\varepsilon_b k_0^2 \sin^2 \theta_l}$ ,  $\gamma_l^b(\kappa_l) = (\varepsilon_b k_0^2 - \kappa_l^2)^{1/2}$ ,  $\gamma(\kappa_l) = (k_0^2 - \kappa_l^2)^{1/2}$  with positive imaginary part,  $r(\kappa_l) = [\gamma^b(\kappa_l) - \gamma(\kappa_l)] / [\gamma^b(\kappa_l) + \gamma(\kappa_l)]$ , and  $t(\kappa_l) = 2\gamma^b(\kappa_l) / [\gamma^b(\kappa_l) + \gamma(\kappa_l)]$ . For  $z \geq 0$  and  $z' \geq 0$ , the Green's function is given by<sup>14</sup>

$$G(\mathbf{r}, \mathbf{r}') = \int \frac{i}{4\pi\gamma(\kappa)} \{ \exp(i\gamma(\kappa)|z - z'|) - r(\kappa) \exp[i\gamma(\kappa)(z + z')] \} \times \exp[i\kappa(x - x')] d\kappa. \quad (6)$$

In the far field along the direction given by the angle  $\theta$  in the superstrate, the Green's function can be approximated as

$$G(\mathbf{r}, \mathbf{r}') = (2\pi/k_0 r)^{1/2} \gamma(\kappa) g(\kappa, \mathbf{r}') \exp(ik_0 r - i\pi/4), \quad (7)$$

where  $r = |\mathbf{r}|$ ,  $\kappa = k_0 x/r = k_0 \sin \theta$  and  $g(\kappa, \mathbf{r}') = [i/4\pi\gamma(\kappa)] \{ \exp[-i\kappa x' - i\gamma(\kappa)z'] - r(\kappa) \exp[-i\kappa x' + i\gamma(\kappa)z'] \}$ . The scattered far field  $e_l^d = E_l - E_l^{\text{ref}}$  can thus be written in the form

$$e_l^d(\mathbf{r}) = E_l^d(\kappa) \exp(ik_0 r) / \sqrt{r}. \quad (8)$$

In a tomography experiment, the phase and amplitude of  $E_l^d(\kappa)$  are measured for various collection angles  $\theta$ . We introduce  $\Gamma$  as the discrete domain of directions of observation. Hereafter,  $\kappa = k_0 \sin \theta$  belongs to  $\Gamma$ . This measurement is performed for successive angles of incidence  $\theta_l$  with  $l = 1, \dots, L$ .

### 3. INVERSION PROCEDURE

The inverse scattering problem consists now in finding the function  $\chi(\mathbf{r} \in \Omega)$  in the investigated area  $\Omega$  (test domain) so that the diffracted field associated with  $\chi$  matches the measured diffracted field  $f_l(\kappa \in \Gamma)$ . Many iterative methods have been developed for solving such inverse problems. In these methods, starting from an initial guess, one adjusts the parameter of interest gradually by minimizing a cost functional involving the measured scattered-field data. A brief review of the literature shows two main approaches. In the first one, namely the linearized methods, the field in the scattering domain is considered fixed. This field is the solution of the forward problem for the best available estimation of the permittivity for each iteration step,<sup>13,15</sup> or it is a reference field if a Born approximation is assumed. In the second approach, typically the modified gradient method, the field inside the scattering domain  $\Omega$  is an unknown that is obtained, together with the permittivity, by the minimization procedure.<sup>16,17</sup> We present herein a hybrid method<sup>12,18</sup> that combines ideas from the two approaches mentioned.

#### A. Principles of the Algorithm

The direct-scattering problem may be formulated as two contrast-source integral relations: (i) the state or obser-

vation equation and (ii) the field or coupling equation. From Eqs. (8), (7), and (3), one gets the observation equation,

$$E_l^d(\kappa \in \Gamma) = \int_{\Omega} k_0^2 \chi(\mathbf{r}') E_l(\mathbf{r}') K(\kappa, \mathbf{r}') d\mathbf{r}', \quad (9)$$

where  $K(\kappa, \mathbf{r}') = (2\pi/k_0) \gamma(\kappa) g(\kappa, \mathbf{r}') \exp(-i\pi/4)$ . For the sake of simplicity, we rewrite the field and observation equations (9) and (3) using operator notation:

$$E_l^d = \mathbf{K} \chi E_l, \quad (10)$$

$$E_l = E_l^{\text{ref}} + \mathbf{G} \chi E_l. \quad (11)$$

The general principle of the modified gradient method for solving this inverse scattering problem is to build up two sequences related to contrast and total field inside the test domain  $\{\chi_n\}$  and  $\{E_{l,n}\}$ , respectively, according to the following recursive relations:

$$E_{l,n} = E_{l,n-1} + \alpha_{l,n} v_{l,n}, \quad (12)$$

$$\chi_n = \chi_{n-1} + \beta_n d_n, \quad (13)$$

where  $v_{l,n}$  and  $d_n$  are search directions with respect to the total field  $E_{l,n}$  and to the contrast, respectively. The choice of these search directions will be discussed in Subsection 3.B. The coefficients  $\alpha_{l,n}$  and  $\beta_n$  are weights that are chosen at each iteration step  $n$  so as to minimize the normalized cost functional  $\mathcal{F}_n(\chi_n, E_{l,n})$  given by

$$\mathcal{F}_n(\chi_n, E_{l,n}) = W_{\Omega} \sum_{l=1}^L \|h_{l,n}^{(1)}\|_{\Omega}^2 + W_{\Gamma} \sum_{l=1}^L \|h_{l,n}^{(2)}\|_{\Gamma}^2, \quad (14)$$

where the normalizing coefficients  $W_{\Omega}$  and  $W_{\Gamma}$  are as follows:

$$W_{\Omega} = \frac{1}{\sum_{l=1}^L \|E_l^{\text{ref}}\|_{\Omega}^2}, \quad W_{\Gamma} = \frac{1}{\sum_{l=1}^L \|f_l\|_{\Gamma}^2}. \quad (15)$$

The subscripts  $\Gamma$  and  $\Omega$  are included in the norm  $\|\cdot\|$  and later in the inner product  $\langle \cdot, \cdot \rangle$  to indicate the domain of integration. The functions  $h_{l,n}^{(1)}$  and  $h_{l,n}^{(2)}$  are two residual errors. The first is the residual error with respect to the incident field in the test domain computed from the field or coupling equation. The second is the error on the scattered field computed from the state or observation equation:

$$h_{l,n}^{(1)} = E_l^{\text{ref}} - E_{l,n-1} + \mathbf{G} \chi_n E_{l,n}, \quad (16)$$

$$h_{l,n}^{(2)} = f_l - \mathbf{K} \chi_n E_{l,n}. \quad (17)$$

The use of *a priori* information may improve the inversion algorithm. For instance, a binary constraint<sup>19</sup> is used to reconstruct the shape of a homogeneous object with known constitutive parameters; nonnegative<sup>20</sup> *a priori* information is applied to a pure imaginary, contrasted object (conducting object); and nonnegative<sup>21</sup> *a priori* information is used to retrieve the shape of a homogeneous object. In the present work, we incorporated *a priori* information stating that the objects are dielectric with no

losses. Instead of retrieving a complex function  $\chi_n$ , only one real auxiliary function  $\xi_n$  is reconstructed such that

$$\chi_n = \xi_n^2. \quad (18)$$

The recursive relation with respect to contrast  $\chi_n$  [Eq. (13)] is then given by

$$\xi_n = \xi_{n-1} + \beta_{n;\xi} d_{n;\xi}. \quad (19)$$

Once the updating directions  $d_{n;\xi}$  and  $v_{l,n}$  are found,  $\mathcal{F}_n$  is a nonlinear expression with  $L$  complex variables ( $\alpha_{l,n;v}$ ) and one real variable ( $\beta_{n;\xi}$ ). The minimization of  $\mathcal{F}_n$  is accomplished using the Polak–Ribière conjugate gradient method.<sup>22</sup>

## B. Search Directions

As updating direction  $d_{n;\xi}$ , we take the standard Polak–Ribière conjugate gradient directions<sup>20,21</sup>

$$d_{n;\xi} = g_{n;\xi} + \gamma_{n;\xi} d_{n-1;\xi},$$

with

$$\gamma_{n;\xi} = \frac{\langle g_{n;\xi}, g_{n;\xi} - g_{n-1;\xi} \rangle_{\Omega}}{\|g_{n-1;\xi}\|_{\Omega}^2}, \quad (20)$$

where  $g_{\xi}$  is the gradient of the cost functional  $\mathcal{F}_n(\xi, E_l)$  with respect to  $\xi$  evaluated at the  $(n-1)$ th step assuming that the total field inside the test domain does not change. This gradient is given by:

$$g_{n;\xi} = 2\xi_{n-1} \operatorname{Re} \left[ W_{\Omega} \sum_{l=1}^L \bar{E}_{l,n-1} \mathbf{G}^{\dagger} h_{l,n-1}^{(1)} - W_{\Gamma} \sum_{l=1}^L \bar{E}_{l,n-1} \mathbf{K}^{\dagger} h_{l,n-1}^{(2)} \right], \quad (21)$$

where the overbar denotes the complex conjugate, and  $\mathbf{G}^{\dagger}$  and  $\mathbf{K}^{\dagger}$  are the adjoint operators of  $\mathbf{G}$  and  $\mathbf{K}$ , respectively.

The search direction  $v_{l,n}$  for the total field inside the test domain is similar to that chosen for the object functions  $\xi$ :

$$v_{l,n} = g_{l,n;E} + \gamma_{l,n;E_l} v_{l,n-1},$$

with

$$\gamma_{l,n;E_l} = \frac{\langle g_{l,n;E_l}, g_{l,n;E_l} - g_{l,n-1;E_l} \rangle_{\Omega}}{\|g_{l,n-1;E_l}\|_{\Omega}^2}, \quad (22)$$

where  $g_{l,n;E_l}$  is the gradient of the cost functional  $\mathcal{F}_n(\xi, E_l)$  with respect to the field  $E_l$  evaluated at the  $(n-1)$ th step, assuming that  $\xi$  does not change, and is given by

$$g_{l,n;E_l} = W_{\Omega} [\bar{\chi}_{n-1} \mathbf{G}^{\dagger} h_{l,n-1}^{(1)} - h_{l,n-1}^{(1)}] - W_{\Gamma} \bar{\chi}_{n-1} \mathbf{K}^{\dagger} h_{l,n-1}^{(2)}. \quad (23)$$

To speed the convergence of the scheme,<sup>12</sup> we modify the inversion procedure by adding a second search direction  $w_{l,n}$  for the total field inside the test domain. The recursive relation (12) with respect to the field  $E_l$  then becomes

$$E_{l,n} = E_{l,n-1} + \alpha_{l,n;v} v_{l,n} + \alpha_{l,n;w} w_{l,n}. \quad (24)$$

The cost function  $\mathcal{F}_n$  is now a nonlinear expression with  $2L$  complex variables ( $\alpha_{l,n;v}$ ,  $\alpha_{l,n;w}$ ) and one real variable

( $\beta_{n;\xi}$ ). The minimization of  $\mathcal{F}_n$  is again accomplished by using the Polak–Ribière conjugate gradient method.<sup>22</sup>

The second updating direction for the total field  $w_{j,n}$  is given by

$$w_{l,n} = \tilde{E}_{l,n-1} - E_{l,n-1},$$

$$\tilde{E}_{l,n-1} = [1 - \mathbf{G}\chi_{n-1}]^{-1} E_l^{\text{inc}}, \quad (25)$$

where  $\tilde{E}_{l,n-1}$  represents the total field inside the test domain  $\Omega$  computed from the coupling equation with contrast  $\chi_{n-1}$ . Adding this search direction provides an acceleration of the algorithm's convergence, at least in terms of number of iterations.<sup>12</sup> On the other hand, it requires solution of the direct problem for a given estimate of the permittivity.

## C. Initial Estimates

Given the *a priori* information that the object function is positive, the initial guess ( $\xi_0 = 0$ ) must be rejected since the gradients vanish ( $g_{1;\xi} = 0$ ). This is due to the transformation (18) which introduces a local maximum of the cost function at  $\xi=0$ . We therefore use another initial guess provided by the backpropagation method.<sup>18–20</sup>

## 4. NUMERICAL RESULTS

In this section, we present reconstructions of the map of index of refraction for different simulated tomography experiments. The scattered far field used as input data for the inversion procedure is calculated by a rigorous volume integral method.<sup>14</sup> The spacing of the mesh is  $\lambda/40$ . The data  $f_l$  of the simulated scattered far field  $E_l^d$  can be artificially corrupted by a Gaussian additive noise as follows:

$$f_l = E_l^d [1 + uA \exp(i\phi)], \quad (26)$$

where  $A = \max_l(|E_l^d|)$ ,  $\phi$  is a random number with uniform probability density between  $[0, 2\pi]$ , and  $u$  is a real number smaller than unity that monitors the noise level. In Fig. 2 we plot the amplitude and phase of typical simulated far-field data with and without 10% noise ( $u = 0.1$ ).

For the reconstruction procedure, the investigation domain  $\Omega$  is a rectangle of width  $2\lambda$  and height  $\lambda/2$  which is meshed with  $\lambda/20$  spacing. This support constraint is a

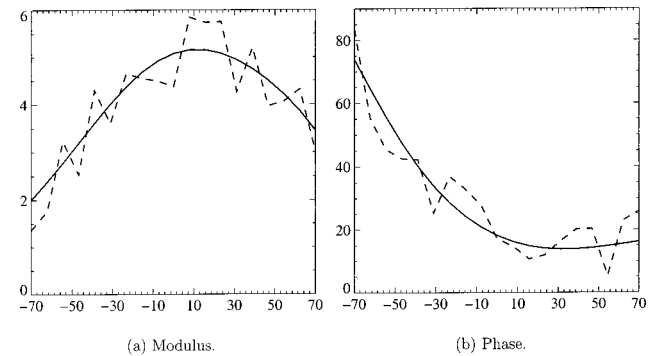
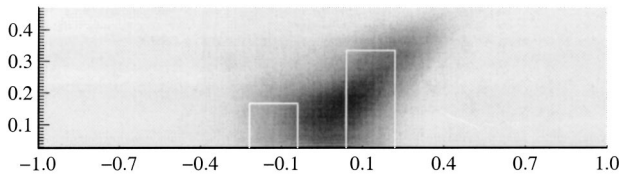
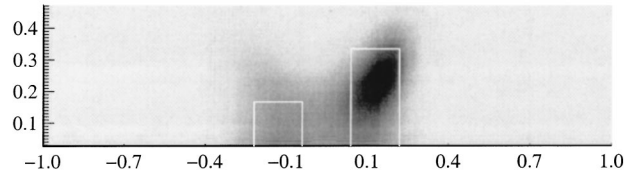


Fig. 2. Scattered far-field modulus (a) and phase (b) versus angles of detection for normal incidence. Noiseless data, bold curve; 10% noise, dashed curve.

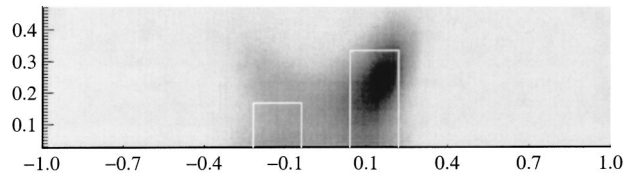


Normal incidence illumination (noiseless data).

Fig. 3. Reconstruction from a single illumination:  $L = 1$ ,  $\theta_1 = 0^\circ$ , and 19 angles of detection ranging from  $-60^\circ$  to  $60^\circ$ . Reconstructed refractive index map in the investigated domain  $\Omega$  with  $2\lambda$  width and  $\lambda/2$  height, represented with gray level.



(a) Noiseless data.



(b) 10% noise.

Fig. 4. Same as in Fig. 3 with 19 angles of incidence ranging from  $-35^\circ$  to  $35^\circ$ .

strong *a priori* piece of information which yields an amelioration of the resolution.<sup>11</sup> Moreover, inversion procedures are more efficient when the number of unknowns, i.e., the permittivity and field at the knots of the mesh, are related to the number of data. With our technique, the number of unknowns should not exceed four times that of the data. Yet in an optical tomography experiment, the illumination spot is much larger than the object (typically several tens of wavelengths if one uses a roughly focalized beam). Hence, we first considered a large domain of width  $30\lambda$  and height  $\lambda/2$  poorly discretized with  $\lambda/2$  spacing to localize the objects with the backpropagating algorithm. Then we reduced the domain of investigation and introduced a more accurate mesh, as described above.

In all experiments, the far field is detected along 19 regularly spaced angles of observation in  $[-60^\circ, 60^\circ]$ . In contrast, the number and angles of the incident directions are different depending on the examples. All reported final results correspond to the 16th iteration of the inverse iterative scheme; this is sufficient, in all cases, for the cost function to reach a plateau.

### A. Mono Incidence

In the first example, the sample is illuminated under normal incidence and  $L = 1$ . The reconstruction is thus performed from 19 complex data. In Fig. 3 we plot the map of the index of refraction of the investigated domain  $\Omega$  after convergence of the algorithm. It is clear that the two objects cannot be distinguished. This calculation

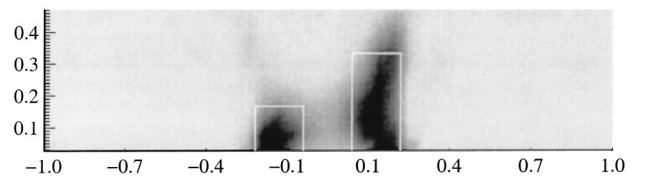
gives a hint of what a classic microscope using only one illumination type can detect. To improve the reconstruction, several incident angles should be used.

### B. Multi-Incidence

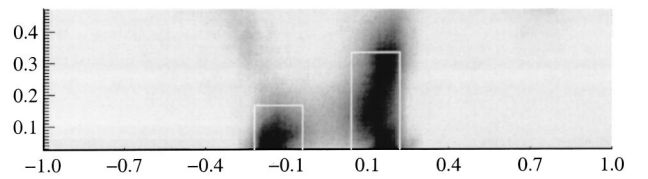
In the second example, 19 incident angles regularly spaced in  $[-35^\circ, 35^\circ]$  are used. The incident angular domain has been chosen so that there is no total internal reflection at the glass–air boundary. In Fig. 4 we now visualize correctly the higher cylinder and localize the smaller one. Outside the small domain surrounding the cylinders, the reconstructed permittivity is equal to 1. There is no oscillation phenomenon. Moreover, it is shown in Fig. 4(b) that imposing 10% noise on the data has a small effect on the reconstruction.

We test in Fig. 5(a) the total-internal-reflection-microscopy configuration. In this case, the incident angles are chosen so that the field is totally reflected at the glass–air boundary. We use 9 incident angles regularly spaced in  $[-70^\circ, -43^\circ]$  and 9 others in  $[43^\circ, 70^\circ]$ . The reconstructed map of permittivity shown in Fig. 5(b) is clearly better than that of the previous example. Both cylinders are now accurately distinguished and their height difference is also detected. This was to be expected since illumination with evanescent waves permits one to explore a larger domain in the Fourier space of the induced currents.<sup>6</sup> The lack of information concerning the low frequencies of the permittivity does not hinder the reconstruction. Yet this configuration seems more sensitive to noise than the previous one. When 10% noise is added to the far-field values, the reconstructed map of permittivity, while remaining correct, is degraded compared with the noiseless estimation.

In Fig. 6 we consider the general configuration when both propagative and evanescent waves illuminate the sample. Nineteen incident angles are taken in  $[-70^\circ, 70^\circ]$ . The advantages of using the complete spectrum of incident waves are patent. Not only is the map reconstructed from noiseless data clearly more accurate than in the second and third examples, but, most important, the sensitivity to noise is strongly reduced. In Fig.



(a) Noiseless data.



(b) 10% noise.

Fig. 5. Same as in Fig. 3 with 18 angles of incidence, 9 of them ranging from  $-70^\circ$  to  $-43^\circ$  and the others ranging from  $43^\circ$  to  $70^\circ$ . All the incident plane waves are totally reflected at the glass–air interface.

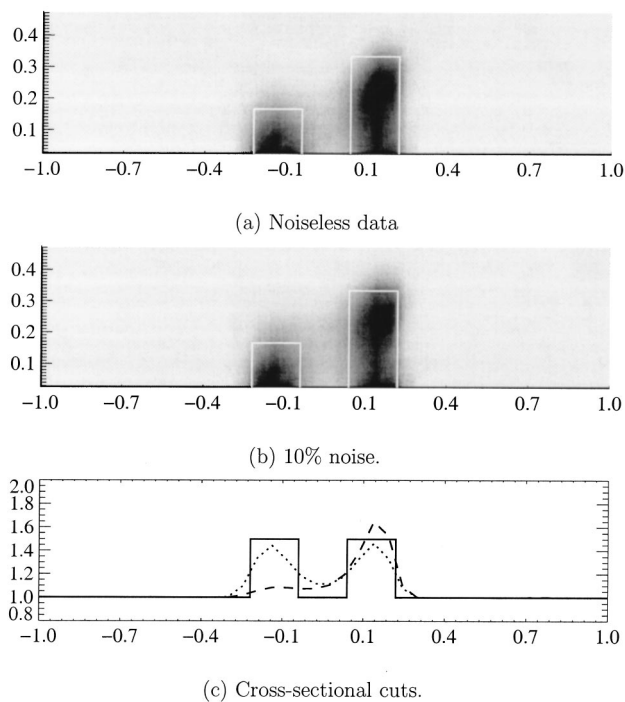


Fig. 6. (a), (b) same as in Fig. 5 with 19 angles of incidence ranging from  $-70^\circ$  to  $70^\circ$ ; (c) cross-sectional cut of the reconstructed refractive index obtained in (b) for two given elevations,  $z = \lambda/10$  (dotted curve) and  $z = \lambda/4$  (dashed curve).

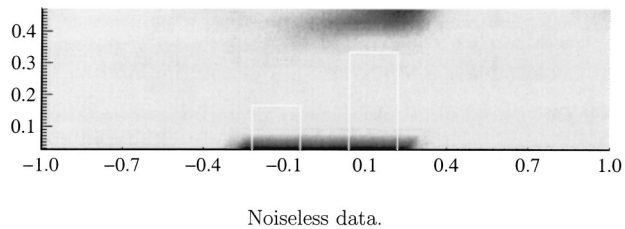


Fig. 7. Same as in Fig. 6(a) but the inversion procedure applies the Born approximation.

6(c) we plot the reconstructed index of refractivity as a function of  $x$  for two given elevations,  $z = \lambda/10$  (dotted curve) when the two objects are present, and  $z = \lambda/4$  (dashed line) when only the higher cylinder is present. Ten percent noise has been added to the data. We see that, in spite of the noise, both cylinders are correctly separated and an accurate value of the index of refraction is obtained. Judging by this example, one can expect a power of resolution better than  $\lambda/5$  in both the lateral and axial directions.

It is worth noting that even though the objects are small and the contrast of refraction index is 0.5, reconstruction procedures using the Born approximation lead to very poor results. In the following example, we consider the general configuration described in the last example (Fig. 6). Assuming the Born approximation is valid, we optimize solely the permittivity through a conjugate gradient scheme. This can be done by calculating directly the inverse operator through singular value decomposition as presented in Ref. 6 or by applying our hybrid technique while keeping  $E_l = E_l^{\text{ref}}$ . The reconstructed map of permittivity obtained with this procedure

is shown in Fig. 7. It shows clearly the advantages of taking into account multiple scattering phenomena.

## 5. CONCLUSION

We have simulated an optical diffraction tomography experiment in which the scattered field of small objects deposited on a substrate is measured along various directions of observation for several successive illuminations. In some configurations, the incident beam from the substrate is totally reflected at the air-glass interface so that the objects are illuminated by an evanescent wave. We propose a reconstruction procedure for retrieval of the map of permittivity of the objects from the data of the scattered field. The objects are two small cylinders (width  $\lambda/6$ , one  $\lambda/6$  high, the other  $\lambda/3$ , and separated by  $\lambda/6$ ) made of glass of  $\varepsilon = 2.25$ . We show that an inverse method assuming the Born approximation leads to poor results in this case. But by using an iterative scheme in which both the permittivity and the electromagnetic field in the objects are modified at each step, it is possible to reconstruct accurately the two cylinders in both the lateral and axial directions. It appears that illumination with evanescent waves ameliorates the accuracy of the reconstruction while illumination with propagative waves diminishes sensitivity to noise. With such a technique, optical diffraction tomography is no longer restricted to weak scatterers and can provide images with subwavelength resolution (below  $\lambda/4$  in air).

Anne Sentenac may be reached by e-mail at [anne.sentenac@fresnel.fr](mailto:anne.sentenac@fresnel.fr).

## ACKNOWLEDGMENT

The authors acknowledge a project grant from the Ministère de la Recherche Française, ACI Jeune Chercheur No. 2115.

## REFERENCES

1. P. S. Carney and J. C. Schotland, "Inverse scattering for near-field microscopy," *Appl. Phys. Lett.* **77**, 2798–2800 (2000).
2. O. Haerlér, A. Dieterlen, and S. Jacquy, "Multiple-objective microscopy with three-dimensional resolution near 100 nm and a long working distance," *Opt. Lett.* **26**, 1684–1686 (2001).
3. J. Enderlein, "Theoretical study of detection of a dipole emitter through an objective with high numerical aperture," *Opt. Lett.* **25**, 634–636 (2000).
4. J.-J. Greffet and R. Carminati, "Image formation in near-field optics," *Prog. Surf. Sci.* **56**, 133–237 (1997).
5. S. B. Ippolito, B. B. Goldberg, and M. S. Ünlü, "High spatial resolution subsurface microscopy," *Appl. Phys. Lett.* **78**, 4071–4073 (2001).
6. P. S. Carney and J. C. Schotland, "Three-dimensional total internal reflection microscopy," *Opt. Lett.* **26**, 1072–1074 (2001).
7. C. M. Blanca, J. Bewersdorf, and S. W. Hell, "Single sharp spot in fluorescence microscopy of two opposing lenses," *Appl. Phys. Lett.* **79**, 2321–2323 (2001).
8. M. Lambert and D. Lesselier, "Binary-constrained inversion of a buried cylindrical obstacle from complete and phaseless magnetic fields," *Inverse Probl.* **16**, 563–576 (2000).
9. V. Lauer, "New approach to optical diffraction tomography

- yielding a vector equation of diffraction tomography and a novel tomographic microscope," *J. Microsc.* **205**, 165–176 (2002).
10. E. Wolf, "Three-dimensional structure determination of semi-transparent objects from holographic data," *Opt. Commun.* **1**, 153–156 (1969).
  11. S. Kawata, O. Nakamura, and S. Minami, "Optical microscope tomography. I. Support constraint," *J. Opt. Soc. Am. A* **4**, 292–297 (1987).
  12. K. Belkebir and A. G. Tijhuis, "Modified<sup>2</sup> gradient method and modified Born method for solving a two-dimensional inverse scattering problem," *Inverse Probl.* **17**, 1671–1688 (2001).
  13. W. C. Chew and Y. M. Wang, "Reconstruction of two-dimensional permittivity distribution using distorted Born iterative method," *IEEE Trans. Med. Imaging* **9**, 218–225 (1990).
  14. J.-J. Greffet, "Scattering of s-polarized electromagnetic waves by a 2D obstacle near an interface," *Opt. Commun.* **72**, 274–278 (1989).
  15. N. Joachimowicz, C. Pichot, and J.-P. Hugonin, "Inverse scattering: an iterative numerical method for electromagnetic imaging," *IEEE Trans. Antennas Propag.* **39**, 1742–1753 (1991).
  16. R. E. Kleinman and P. M. van den Berg, "A modified gradient method for two-dimensional problems in tomography," *J. Comput. Appl. Math.* **42**, 17–35 (1992).
  17. R. E. Kleinman and P. M. van den Berg, "An extended range-modified gradient technique for profile inversion," *Radio Sci.* **28**, 877–884 (1993).
  18. K. Belkebir, S. Bonnard, F. Pezin, P. Sabouroux, and M. Saillard, "Validation of 2D inverse scattering algorithms from multi-frequency experimental data," *J. Electromagn. Waves Appl.* **14**, 1637–1667 (2000).
  19. L. Souriau, B. Duchène, D. Lesselier, and R. E. Kleinman, "Modified gradient approach to inverse scattering for binary objects in stratified media," *Inverse Probl.* **12**, 463–481 (1996).
  20. R. E. Kleinman and P. M. van den Berg, "Two-dimensional location and shape reconstruction," *Radio Sci.* **29**, 1157–1169 (1994).
  21. K. Belkebir, R. E. Kleinman, and C. Pichot, "Microwave imaging: Location and shape reconstruction from multifrequency scattering data," *IEEE Trans. Microwave Theory Tech.* **45**, 469–476 (1997).
  22. W. H. Press, B. P. Flannery, S. A. Teukolski, and W. T. Vetterling, *Numerical Recipes: The Art of Scientific Computing* (Cambridge University, Cambridge, UK, 1986).